ELSEVIER

Journal of Structural Geology 29 (2007) 1679–1694

JOURNAL OF STRUCTURAL GEOLOGY

www.elsevier.com/locate/jsg

Numerical investigation of localization and micromechanics in a stratified soil specimen

Ingo Kock*, Katrin Huhn

DFG Research Center Ocean Margins, Leobener Street, D-28359 Bremen, Germany

Received 9 November 2006; received in revised form 12 July 2007; accepted 17 July 2007
Available online 2 August 2007

Abstract

For many geological deformation processes the existence of a mechanically weak layer is assumed. For these weak layers, clay sediments or clayey fault gouge seem to be likely candidates. They are supposed to be a focus of displacement and thus crucial for slip plane and shear zone development. There is an ongoing debate concerning the exact nature of shear localization in these layers. To address this question, we use numerical shear box tests utilizing the Discrete Element Method (DEM). Our focus lies on the localization patterns and micromechanical properties of stratified 'silt'–'clay'–'silt' and 'clay'–'clay'–'clay' specimens. We systematically vary the mechanical strength of each layer via the coefficient of particle friction to analyse localization and the micromechanics of the material.

Our results indicate that the deformation of a material package is the result of different deformation modes. The ability of single particles to slide, roll or rotate is influenced to a large extent by layer strength and particle friction, which also govern the layers' ability to dilate or contract during deformation. We show that the localization switches from a given layer to adjacent layers even if differences in the material properties are very small. Furthermore, the localization is often concentrated in only one layer leading to a complete decoupling of the other layers and thus building a shear zone where high displacement can be accumulated.

Keywords: DEM; Localization; Shear; Micromechanics; Soil; Numerical modelling

1. Introduction

Shearing processes at the upper brittle crust are attributed to the existence of mechanically weak layers. These are characterized by a lower shear or frictional strength which can be explained by their lithology compared to the surrounding materials (Dahlen, 1984; Hampton et al., 1996). Clay sediments, therefore, exhibit lower shear strength compared to silts (Mitchell and Soga, 2005). In addition, Lupini et al. (1981) and Huhn et al. (2006) have shown a direct relationship between clay size fraction and the shear strength of sediments. Besides physicochemical reactions, interactions of water, etc., the grain shape of tabular clay minerals is one reason for the low frictional strength. To be more precise, it is the alignment of platy clay minerals during shear deformation and the breakdown of the microstructure (Mitchell and Soga, 2005).

As sediments can be considered as a granular material, grain–grain interactions are responsible for the deformational behaviour (Oda and Iwashita, 1999; Mitchell and Soga, 2005). Grain sliding, rolling, and rotation are microscopic deformation modes that influence the micromechanics and microstructural evolution. For example, the distribution of stresses is not homogenous in a granular material and some grains carry more load than others (e.g. Jaeger et al., 1996).

In nature, numerous distinct shear planes are formed and reactivated repeatedly creating a shear zone. In addition, weak layers are not homogenous stratigraphic units, thus, deformation takes place in well-defined parts of a stratified sediment, even if the whole package belongs to a shear zone (Labaume et al., 1997; Maltman et al., 1997; Canals et al., 2004). A highly resolved spatio-temporal description of shear zone development

* Corresponding author. Tel.: +49 241 65862.
E-mail address: ikock@uni-bremen.de (I. Kock).

0191-8141/$ - see front matter © 2007 Elsevier Ltd. All rights reserved.
doi:10.1016/j.jsg.2007.07.013

is, however, difficult to construct both in nature and under laboratory conditions. To date, the role of stratification in shear zone evolution is unknown. For a shear zone it is still uncertain if the localized deformation is related to the stratification. A detailed description and analysis of how shear localizes in a weak layer needs to be performed on a microscopic scale.

The aim of this paper is to gain a deeper insight into microscopic shear zone evolution in stratified sediments. Specifically, how do strength contrasts in a horizontally layered specimen influence the localization phenomena, and in particular, do shear planes form directly at layer boundaries or alternatively at the top, middle, or basal part of a weak sediment package? Therefore, we study the micromechanics of shear zone development at the grain scale level using a numerical shear box experiment. We utilize the Discrete Element Method (DEM) to investigate shear stress evolution and deformation styles of stratified sediments. Two types of horizontally layered specimen were simulated: (1) a 'silt'–'clay'–'silt' assemblage and (2) a 'clay'–'clay'–'clay' package.

As a first step, we quantified the mechanical strength of homogenous particle assemblies as a function of the coefficient of particle friction, this enabled the calculation of strength ratios for the stratified experiments. Within these stratified assemblies we varied systematically the particle friction for a given layer and thus the strength ratio between the layers. We focus on (1) slip plane and shear zone evolution and (2) shear stress development, the percentage of slipping grains (sliding fraction) and the magnitude of grain rolling and rotation.

2. Methods

2.1. The Discrete Element Method

The Discrete Element Method is based upon a numerical description of granular materials. This study employed the commercial 2D code PFC2D, which was developed by Cundall and Strack (1978). A sufficiently large particle assemblage (e.g. ~800 in this case; Table 1; Fig. 1) can reproduce deformation behaviour similar to that occurring in various types of sediments, soils, and rocks. For example, numerical modelling of granular material with DEM was used to investigate fault gouge mechanics (Morgan, 1999; Morgan and Boettcher, 1999), fault propagation (Schöpfer et al., 2006), fault evolution of mixed sediments (Huhn et al., 2006), and the influence of particle shape on shear zone development and frictional strength (Kock and Huhn, 2007).

In the DEM model, circular particles interact according to simple physical contact laws and the microproperties of each particle, such as the particle coefficient of friction $\mu_{(P)}$, which control the particle–particle interactions must be defined. The overall mechanical and physical behaviours of the particle assemblage itself are the result of all particle interactions. Therefore, the macroproperties or overall properties of a particle assemblage have to be calculated, e.g. average shear stress.

Limitations of 2D mainly concern unreasonably low macroscopic shear stresses with relatively high fluctuations (e.g. Morgan, 1999; Mair et al., 2002). It has been shown that these effects are reduced in 3D simulations (Hazzard and Mair, 2003). However, 3D simulations require a large amount of computation time whilst a suite of simulations may be run in 2D in a reasonable amount of time.

A complete review of the DEM algorithms would exceed the scope of this paper. However, the numerical description of the code is described completely by Cundall and Strack (1978, 1979, 1983), Cundall (1989) and Itasca (2004). Short reviews are given in Antonellini and Pollard (1995), Morgan and Boettcher (1999) and Kock and Huhn (2007). Furthermore, it must be mentioned that in our simulations the influence of fluids, grain fracture and gravitational forces have not been taken into account.

Table 1
Properties and configuration of numerical models

	Experiment I	Experiment II
Shear box properties		
Width [μm]	200	200
Height [μm]	140 (initial)	140 (initial)
Normal stress σ_N [Pa]	5×10^6	5×10^6
Shear velocity [μm/s]	6	6
Particle number: 'Silt'	162	0
Tabular particle number: 'Clay'	624	1872
Particle properties		
Normal stiffness, k_N [N/m]	1×10^9	1×10^9
Shear stiffness, k_S [N/m]	1×10^9	1×10^9
Density, ρ [kg/m^3]	*	*
Diameter [μm]: 'Silt'	5.6–20	
Diameter [μm]: 'Clay'	Short axis: 2 Long axis: 6	Short axis: 2 Long axis: 6
Particle friction $\mu_{(P)}$ range:	0.05–1.0	0.05–1.0

*density is only relevant to compute the internal timestep and need not to be realistic and therefore is scaled to an unrealistic high value to achieve a higher computing time.

2.2. Numerical shear box configuration

Consistent with analogue shear box experiments (e.g. Saffer et al., 2001; Kopf and Brown, 2003; Saffer and Marone, 2003; Ask and Kopf, 2004) and other numerical DEM simulations (e.g. Morgan, 1999; Morgan and Boettcher, 1999; Guo and Morgan, 2004; Huhn et al., 2006; Kock and Huhn, 2007), we developed a 2D numerical shear box (Fig. 1; Table 1).

The lower and upper boundary walls of the shear box consisted of 10 particles with a diameter of 20 μm and thus formed a box with a total width of 200 μm. The lower wall remained fixed in the x- and y-directions throughout all of the experiments. The upper wall could move in the x- and y-directions to induce shear ($\tau_{(M)}$) and normal stress ($\sigma_{N,(M)}$) (Fig. 1). In order to be comparable to laboratory experiments (e.g. Mair et al., 2002), the shear rate and the normal stress were held constant at 1 μm/s and 5 MPa, respectively, using servo algorithms applied to the upper wall. Hence, depending on the sheared materials, shear box height was variable during each experimental run, starting from an initial height of 140 μm. To achieve large quantities of strain (200%), the left and right

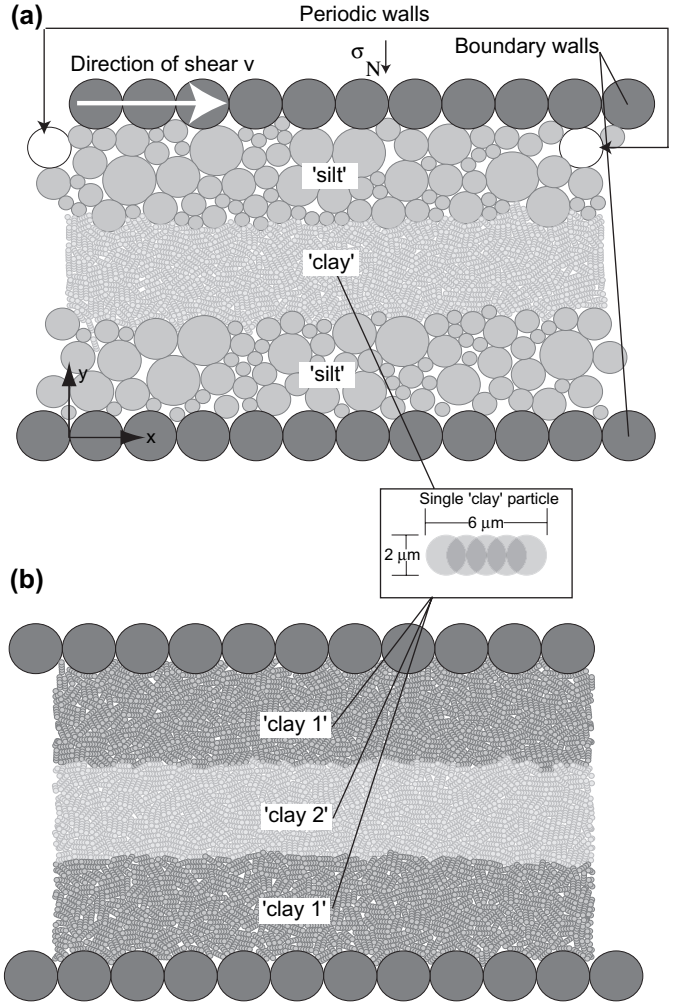

Fig. 1. Model of both 2D shear box experiments. The middle box shows 'clay' particles built of five circular particles. The arrows indicate the periodic feature of the box: both white particles on either side are the same particle. (a) Indicated in medium grey is the 'silt', built out of circular particles. Dark grey are boundary particles 'walls'. 'Clay' particles appear in light grey. (b) Indicated in medium grey are the top and bottom layer 'clay'. Dark grey are boundary particles 'walls'. 'Clay' particles of the intermediate layer appear in light grey. 'Clay' particle shape and properties of all layers are equal, except particle friction for the intermediate layer.

box boundaries were periodic, thus, any particles which moved out of the right hand side of the box reappeared on the left hand side and vice versa.

As natural 'silt' grains appear to be approximately circular in shape (Bennett et al., 1991), the numerical 'silt' is simulated using perfectly circular particles, whose diameters are log-normally distributed (e.g. Tucker, 1981; Füchtbauer, 1988) between 5.6 and 20 µm with a peak value at 10 µm. In contrast, natural clays typically have a tabular, platy structure (Bennett et al., 1991; Mitchell and Soga, 2005). Therefore, circular particles were connected to simulate elongated grains. These 'clay grains' were constructed from five circular particles combined together with fixed relative positions (Fig. 1). This grain type has been successfully used to simulate normally consolidated 'clay' sediments (Kock and Huhn, 2007) and 'clay–silt' mixtures (Huhn et al., 2006).

Initially, each particle type (circular or elongated) was used to create homogenous 'clay' or 'silt' materials that were employed in reference simulations (Table 2). During any given simulation, the particle coefficient of friction, $\mu_{(P)}$, remained constant and after completion the macroscopic shear strength of the material was calculated. The particle coefficient of friction was varied between simulations and thus, a direct relationship between the coefficient of particle friction $\mu_{(P)}$ and the associated shear strength could be determined.

Based on these homogenous control simulations, the strength ratio (SR) between different homogenous layers (with a specific coefficient of particle friction $\mu_{(P)}$) could be computed for each stratified model ('silt'–'clay'–'silt'; 'clay'–'clay'–'clay', Table 3). Strength ratios <1.0 indicate that the intermediate material has a shear strength lower than the under and overlying layers, whilst strength ratios >1.0 indicate the opposite situation.

Stratified experiments included:

(I) A study of the deformational behaviour of stratified 'sediments' with distinct lithological boundaries. Hence, a numerical 'clay' layer was intercalated between two 'silt' layers (Fig. 1a). In this setting different strength ratios were tested. We distinguished:

(Ia) A constant value of 0.1 was employed for the microscopic coefficient of friction $\mu_{(P)}$ of the 'clay', whilst $\mu_{(P)}$ for the 'silt' layers was varied between the simulations in the range 0.01–1.0 (experiments Ia-1 to Ia-9; Table 3).

(Ib) $\mu_{(P)}$ for the 'silt' was held constant at 0.2, whereas $\mu_{(P)}$ for the 'clay' changed from 0.01 to 1.0 (experiments Ib-1 to Ib-9; Table 3).

Table 2
Stress ratios (measured shear vs. measured normal stress) for reference experiments

Experiment	$\mu_{(P)}$	Peak stress ratio	Average stress ratio	Standard deviation
Reference 'Silt'				
R1	0.01	0.12	0.09	0.01
R2	0.05	0.18	0.14	0.02
R3	0.1	0.22	0.18	0.02
R4	0.2	0.34	0.24	0.03
R5	0.3	0.39	0.27	0.04
R6	0.4	0.43	0.26	0.04
R7	0.5	0.46	0.26	0.05
R8	0.75	0.52	0.27	0.06
R9	1.0	0.56	0.26	0.06
Reference 'Clay'				
R10	0.01	0.29	0.22	0.06
R11	0.05	0.32	0.26	0.06
R12	0.1	0.35	0.28	0.06
R13	0.2	0.37	0.32	0.07
R14	0.3	0.418	0.36	0.07
R15	0.4	0.417	0.37	0.07
R16	0.5	0.43	0.37	0.07
R17	0.75	0.46	0.39	0.07
R18	1.0	0.49	0.37	0.10

Table 3
Particle friction variation and strength ratios for stratified assemblies

Experiment	$\mu_{(P)}$ (top and bottom layer)	$\mu_{(P)}$ (intermediate layer)	Equivalent materials from Table 2	Strength ratio
Ia-1	0.01	0.1	R12/R1	2.95
Ia-2	0.05	0.1	R12/R2	1.91
Ia-3	0.1	0.1	R12/R3	1.58
Ia-4	0.2	0.1	R12/R4	1.02
Ia-5	0.3	0.1	R12/R5	0.89
Ia-6	0.4	0.1	R12/R6	0.80
Ia-7	0.5	0.1	R12/R7	0.75
Ia-8	0.75	0.1	R12/R8	0.66
Ia-9	1.0	0.1	R12/R9	0.62
Ib-1	0.2	0.01	R10/R4	0.86
Ib-2	0.2	0.05	R11/R4	0.92
Ib-3	0.2	0.1	R12/R4	1.02
Ib-4	0.2	0.2	R13/R4	1.10
Ib-5	0.2	0.3	R14/R4	1.23
Ib-6	0.2	0.4	R15/R4	1.22
Ib-7	0.2	0.5	R16/R4	1.26
Ib-8	0.2	0.75	R17/R4	1.34
Ib-9	0.2	1.0	R18/R4	1.45
II-1	0.1	0.01	R10/R3	0.84
II-2	0.1	0.05	R11/R3	0.91
II-3	0.1	0.1	R12/R3	1.00
II-4	0.1	0.2	R13/R3	1.08
II-5	0.1	0.3	R14/R3	1.21
II-6	0.1	0.4	R15/R3	1.20
II-7	0.1	0.5	R16/R3	1.24
II-8	0.1	0.75	R17/R3	1.32
II-9	0.1	1.0	R18/R3	1.42

Strength ratio is defined as: SR = shear strength$_{(int.\ layer)}$/shear strength$_{(top\ and\ bot.\ layer)}$ and is calculated from the values presented in Table 2.

Therefore, in experiment I different strength ratios were achieved for each simulation. Additionally, in some cases the strength of the 'silt' is smaller than that of 'clay' resulting in an SR > 1 (see Table 3), which could represent the case of a weak soil overlaying cemented clay or welded volcanic ash.

(II) To examine the deformation of sediments not stratified in terms of their lithology but rather by differences in their material properties, we used a pure 'clay' assemblage (Fig. 1b). Hence, in this experiment a stratum of 'clay' was intercalated between two further 'clay' layers. In a similar manner to experiment (I), different strength ratios were tested. The microproperties of all the 'clay' particles were identical, except the intermediate 'clay' layer where $\mu_{(P)}$ was changed from 0.01 to 1.0. For the upper and lower layers, $\mu_{(P)}$ was held constant at 0.1 (experiments II-1 to II-9; Table 2).

2.3. Analyse and interpretation techniques

Throughout the experiments shear strains of up to 200% were achieved, whilst various different parameters and macroscopic material properties were measured:

- The shear and normal stresses acting on the particles were computed at each 1% increment of the strain. It is important to note that we calculated the average shear stress acting on the particles, which is in contrast to previous studies that measured the shear stress inside a specified volume of material (e.g. Kock and Huhn, 2007; as outlined in Itasca, 2004). This calculation was performed for the pure 'silt' and 'clay' assemblages as well as for each separate layer in the stratified experiments. Consequently, shear stress curves could be calculated from 0% to 200% strain. From these curves the peak (maximum amplitude), average and standard deviation of the shear stress could be calculated. Computation of the standard deviation was necessary to assess the variations in the 'silt' layers which may be high due to the relatively low particle number. For examples of shear and normal stress evolution during deformation see the Appendix.

For the pure assemblies, shear strength was calculated by taking the maximum ratio of the shear to the normal stress. Strength ratios (SR) could then be calculated using the values discussed above (Table 3).

- Displacement of each particle in the x- and y-directions was recorded continuously. In a manner similar to Morgan and Boettcher (1999), the vertical gradient of the horizontal displacement field could be calculated and then plotted with GMT (Wessel and Smith, 1991). These displacement gradients monitor internal deformation and mark the position and angle of slip planes and shear zones (Morgan and Boettcher, 1999; Guo and Morgan, 2004; Huhn et al., 2006; Kock and Huhn, 2007).
- The percentage of slipping contacts was monitored at 1% increments in the strain. Hence, the average value and standard deviation could be computed after reaching 200% strain. Below, we use the term 'sliding fraction' for this parameter. Simultaneously, we recorded the angle of rotation for each of the particles. We distinguished between rolling for the circular 'silt' particles and rotation for the elongated 'clay' particles, because they represent different deformation modes (Kock and Huhn, 2007). During deformation, circular particles may rotate while remaining in the same position, whereas platy 'clay' particles only rotate when there is enough space available for the long axis to rotate. We calculated (a) the portion of the 'silt' grains that experienced finite rolling and (b) the amount of 'clay grains' which rotated more than 30°, 60°, 90°, or 180°. Based on the slipping and rolling values, we were able to distinguish the different deformation behaviours between the layers (sliding, rolling, and rotation).

3. Results

3.1. Homogenous models

3.1.1. Pure 'silt' experiments

Shear stress evolution showed a strong dependency on the particle coefficient of friction (Fig. 2a). Peak values of the

shear stress ratio ranged from 0.12 to 0.56 with the average ratio varying from 0.09 to 0.26. In general, an increase in the peak stress ratio would be observed with increasing $\mu_{(P)}$ (Fig. 2b; Table 2), whereas the average stress ratio approached a constant threshold. Despite using a different measurement technique, values for the average stress ratio are similar to those of Morgan (1999).

3.1.2. Pure 'clay'

Evolution of the shear stress for the pure 'clay' assemblages differed greatly from the 'silt' experiments (Fig. 2c,d; Table 2). Curves for the 'clay' were smoother and showed a slower increase to peak stress ratios. In a similar manner to the pure 'silt', both stress ratios increased when $\mu_{(P)}$ was increased, albeit non-linearly, to a maximum value of 0.49 for the peak stress. Peak stress ratios were, however, lower for high $\mu_{(P)}$, but the average stress ratios were higher compared to the 'silt' experiment.

3.1.3. Calculation of strength ratios

Based on the variation of $\mu_{(P)}$ for homogenous materials, a wide spectrum of strength ratios was determined for the stratified materials (Table 3). Ratios <1.0 indicate that the intermediate layer was mechanically weaker than its neighbours, whereas ratios >1.0 correspond to a strong embedded interlayer. Note that the calculation of the strength ratios implies that the coefficient of particle friction between the layers may be equal, even when the SR is not.

For experiments Ia and Ib, values of SR ranged between 0.62 and 2.95. In general, values in experiment Ia were widely distributed corresponding to strong and weak 'clayey' interlayers. In experiment Ib, values were mostly >1.0 indicating the 'silt' to be the mechanically weak material. Similarly, in experiment II, values of SR were obtained in the range 0.84–1.42. Hence, in experiment II the weak layer always had the lowest coefficient of particle friction.

3.2. Localization features

3.2.1. Variation of $\mu_{(P)}$ (SR) for 'silt' in experiment Ia

Variation of $\mu_{(P)}$ of the 'silt' particles and its influence on SR resulted in different shear planes and shear zone geometries (Fig. 3a,i–v).

A high strength ratio (SR $\sim$ 3), when $\mu_{(P),\text{'silt'}} << \mu_{(P),\text{'clay'}}$, showed long shear planes mainly located in the upper 'silt' layer (Fig. 3a,i), whereas only a few short shear planes could be observed inside the intermediate 'clays'. No internal deformation was observed in the lower 'silt'. Shear planes in the upper 'silt' were inclined $\sim\pm25^\circ$ from the horizontal and in some cases, single shear planes were connected. However, no coherent shear zone was observed that extended over the entire shear box.

A decrease of SR to values of $\sim$2 resulted in an increase of deformation in the intermediate 'clay' layer (Fig. 3a,ii). Nevertheless, the majority of the slip planes still occurred in the top 'silt' layer, whilst shear plane geometry remained constant.

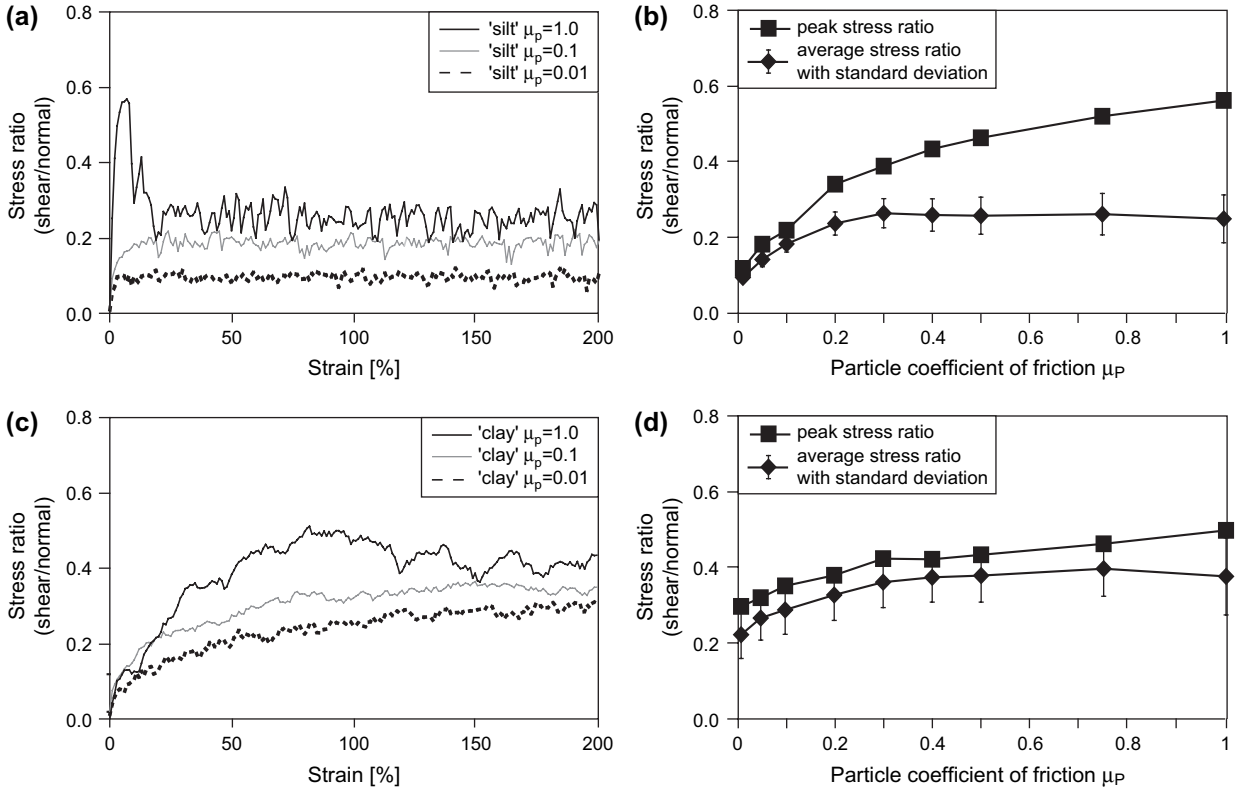

Fig. 2. Stress ratios for homogenous assemblages. (a) Selected stress ratio curves for 'silt'. (b) Peak and average stress ratio with standard deviations after 200% strain for 'silt'. (c) Selected stress ratio curves for 'clay'. (d) Peak and average stress ratio with standard deviations after 200% strain for 'clay'.

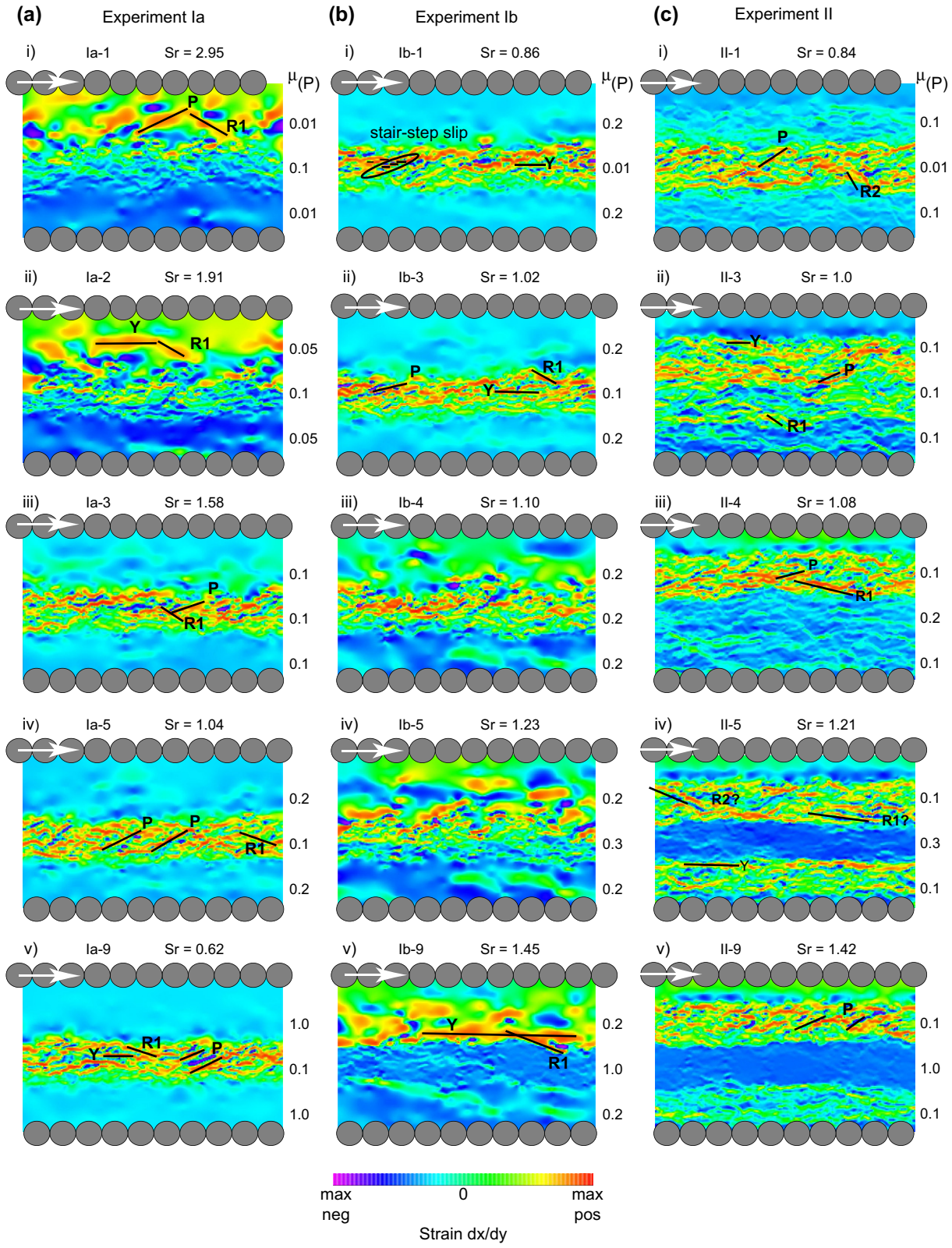

Fig. 3. Gradient of horizontal displacement. Red colours indicate maximum positive relative displacement, magenta indicates maximum negative relative displacement. Note that displacement is relative and not absolute, so that even for particles showing as magenta, absolute net displacement in positive x-direction >0. Black bars indicate some selected slip planes. Slip plane notation after Rutter et al. (1986). Black ellipse shows a stair-step structure. Strength ratio SR is indicated above and particle friction on the right of each plot. (a) Experiment Ia: variation of strength via particle friction coefficient of 'silt' of the top and bottom layer. Strength (and particle coefficient of friction) for 'clay' in the intermediate layer is constant. Specimen design is: 'silt', top and bottom layer; 'clay', intermediate layer. (b) Experiment Ib: variation of strength via particle friction coefficient of 'clay' of the intermediate layer. Strength (and particle coefficient of friction) for 'silt' is constant in the top and bottom layer. Specimen design is: 'silt', top and bottom layer; 'clay', intermediate layer. (c) Experiment II: variation of strength via particle friction coefficient of 'clay' of the intermediate layer. Strength (and particle coefficient of friction) for 'clay' is constant in the top and bottom layer. Specimen design is: 'clay', top, intermediate and bottom layer (for interpretation of the color in the text, the reader is referred to the web version of the article).

Further decreases in SR led to a complete change in the deformation (Fig. 3a,iii). Nearly all shear planes were located inside the 'clay' layer, although a strength ratio of 1.58 indicates that the 'silt' remained the mechanically weak layer. There was little indication of internal deformation in the upper 'silt' layer, and even less in the lower one. Shear planes in the 'clay' layer were narrower and shorter compared to those of the previous experiments. Here, long shear zones evolved that extended over more than half of the width of the shear box (Fig. 3a,iii). The shear plane inclinations were distributed between −50° and +50°.

Continued decrease of SR had no effect on the localization features (Fig. 3a,iv–v), with the exception of the shear zone geometry, which was more pronounced than in the previous models.

3.2.2. Variation of $\mu_{(P)}$ (SR) for 'clay' in experiment Ib

Variation of $\mu_{(P)}$ of the 'clay' also controlled the geometry of the shear planes and therefore the shear zone localization (Fig. 3b,i–v). Additionally, this suite of experiments exhibited the same trends for localization in relation to SR as observed in experiment Ia.

In the case of low strength ratios (SR < 1.0), the shear planes were localized exclusively in the intermediate 'clay' layer (Fig. 3b,i–ii). The shear planes were long and narrow with many interconnections, resulting in a focused shear zone. In general, shear plane position and geometry were similar to experiments Ia-5 to Ia-9, where also the strength ratio was very low (Fig. 3a,iv–v).

An increase of SR to values >1.1 resulted in a shear plane localization shift towards the upper and also, to a lesser extent, lower 'silt' layer (Fig. 3b,iii–iv). A distinct shear zone within the 'clay' layer was no longer visible. When the strength ratio was highest (SR = 1.45), a long and broad shear plane was visible just on top of the 'clay', at the base of the 'silt' (Fig. 3b,v).

3.2.3. Variation of $\mu_{(P)}$ of the intermediate 'clay' in experiment II

In contrast to the former experiments, variation of $\mu_{(P)}$ of the 'clay' and therefore the SR controls only shear zone localization, whereas shear plane geometry remained constant.

A strength ratio of SR < 1.0 resulted in a distinctly coherent shear zone located inside the intermediate 'clay' layer (Fig. 3c,i). Its shape was in general comparable to that in experiment Ib-1 (Fig. 3b,i). Simultaneously, the top layer showed less developed shear planes.

The subsequent increase of the SR to 1.0 showed a broadening of the shear zone localization into the upper layer where the majority of the shear planes were located (Fig. 3c,ii). No distinct border in deformation behaviour between different 'clay' layers could be detected.

Additional increases of the SR to values >1.0 resulted in a shear zone localized completely in the top 'clay'. Equivalently, internal deformation in the intermediate and bottom layers (Fig. 3c,iii) was almost non-observable.

Further increases of the SR produced no internal deformation in the intermediate layer (Fig. 3c,iv–v). Shear plane localization was mainly concentrated in the upper and to a lesser degree in the bottom layer.

3.3. Average shear stress

Variation of the microscopic coefficient of particle friction $\mu_{(P)}$ of the 'silt' particles and the associated change of the strength ratio influenced shear stress response at the particle level (Fig. 4; Table 4).

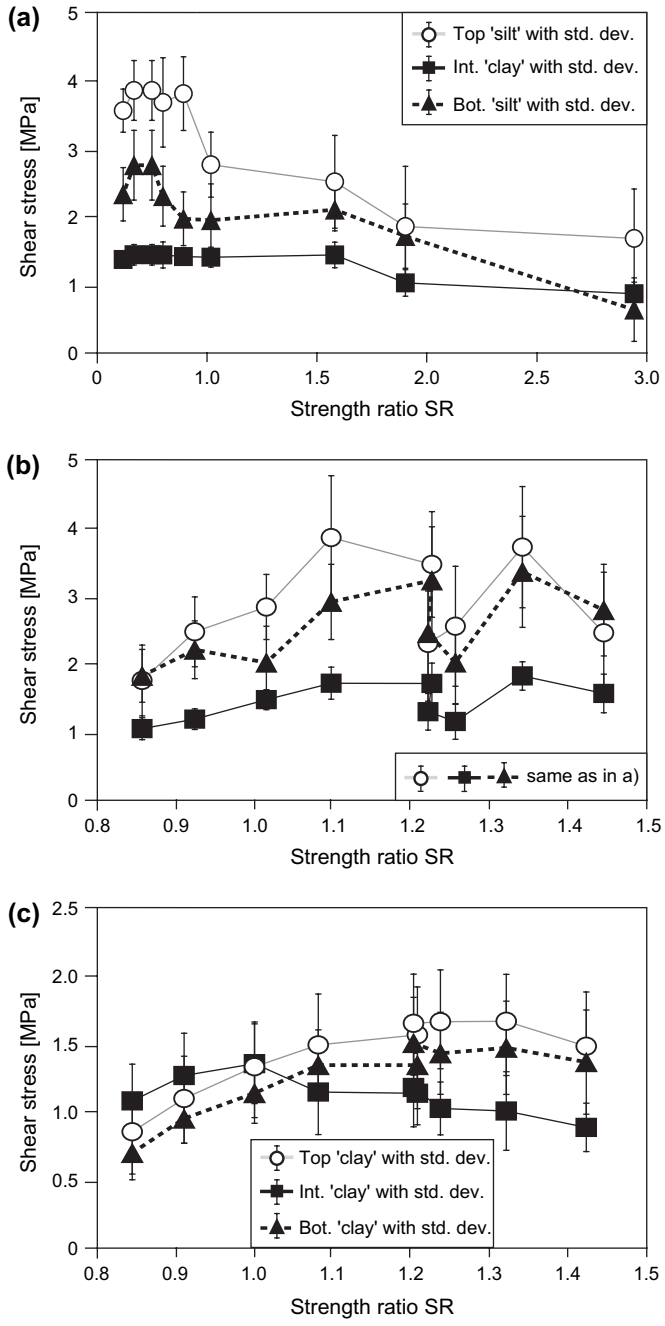

Fig. 4. Shear stress vs. strength ratio SR. Shear stress is the average particle shear stress from 0% to 200% strain. Circles denote shear stress for the top layer, squares for the intermediate layer, and triangles for the bottom layer. (a), (b), and (c) are same as Fig. 3.

Table 4
Overview of selected results

Exp.	Boundary conditions			Results									
	Particle friction			Average shear stress [MPa]			Sliding fraction [%]			Rotation > 30° [%]		Rotation > 180° [%]	
	Top and bot.	Int.	SR	Top	Int.	Bot.	Top	Int.	Bot.	Top and bot.	Int.	Top and bot.	Int.
Ia-1	0.01	0.1	2.95	**1.74**	0.92	*0.69*	**51**	*26*	33	**52.1**	*50.6*	**10.4**	0
Ia-2	0.05	0.1	1.91	**1.91**	*1.08*	1.77	**35**	24	*23*	**65.0**	*60.3*	**7.4**	0
Ia-3	0.1	0.1	1.58	**2.57**	*1.49*	2.16	17	**25**	*12*	*40.5*	**60.7**	**1.2**	0
Ia-4	0.2	0.1	1.02	**2.82**	*1.46*	2.00	14	**25**	*11*	*47.9*	**60.4**	**1.8**	0
Ia-5	0.3	0.1	0.89	**3.87**	*1.47*	2.03	*9*	**27**	12	*44.2*	**63.3**	**1.8**	0
Ia-6	0.4	0.1	0.80	**3.74**	*1.49*	2.36	12	**27**	*9*	*46.6*	**65.2**	**3.1**	0
Ia-7	0.5	0.1	0.75	**3.91**	*1.50*	2.81	*6*	**27**	8	*35.0*	**59.5**	**1.2**	0
Ia-8	0.75	0.1	0.66	**3.91**	*1.50*	2.81	7	**27**	*5*	*39.3*	**60.9**	**1.8**	0
Ia-9	1.0	0.1	0.62	**3.62**	*1.48*	2.65	5	**28**	*2*	*16.0*	**60.7**	**0.6**	0
Ib-1	0.2	0.01	0.86	1.74	*1.03*	**1.81**	21	**61**	*18*	*25.2*	**63.6**	**1.8**	0
Ib-2	0.2	0.05	0.92	**2.46**	*1.17*	2.19	22	**38**	*16*	*38.0*	**61.7**	**2.5**	0
Ib-3	0.2	0.1	1.02	**2.82**	*1.46*	2.00	14	**25**	*11*	*47.9*	**60.4**	**1.8**	0
Ib-4	0.2	0.2	1.10	**3.84**	*1.70*	2.90	**20**	16	*14*	*64.4*	**64.6**	**5.5**	0
Ib-5	0.2	0.3	1.23	**3.45**	*1.70*	3.21	**21**	*12*	15	**77.9**	*64.9*	**10.4**	0
Ib-6	0.2	0.4	1.22	2.29	*1.28*	**2.44**	**33**	*7*	20	**65.0**	*39.6*	**11.7**	0
Ib-7	0.2	0.5	1.26	**2.54**	*1.14*	2.01	**32**	*7*	15	**57.1**	*32.4*	**17.2**	0
Ib-8	0.2	0.75	1.34	**3.70**	*1.81*	3.34	**19**	*5*	15	**76.7**	*51.4*	**14.7**	0
Ib-9	0.2	1.0	1.45	2.44	*1.55*	**2.78**	**30**	*3*	17	**66.3**	*31.1*	**19.0**	0
II-1	0.1	0.01	0.84	0.85	**1.08**	*0.70*	*13*	**57**	16	*26.8*	**60.1**	0	0
II-2	0.1	0.05	0.91	1.10	**1.26**	*0.95*	*18*	**37**	19	*36.5*	**59.0**	0	0
II-3	0.1	0.1	1.00	1.33	**1.35**	*1.14*	**26**	25	*23*	*45.3*	**55.0**	0	0
II-4	0.1	0.2	1.08	**1.49**	*1.14*	1.34	**30**	*15*	21	**52.0**	*40.1*	0	0
II-5	0.1	0.3	1.21	**1.56**	*1.13*	1.34	25	*7*	**27**	**54.6**	*19.9*	0	0
II-6	0.1	0.4	1.20	**1.65**	*1.18*	1.50	**27**	*6*	25	**56.8**	*17.8*	0	0
II-7	0.1	0.5	1.24	**1.66**	*1.02*	1.43	**30**	*4*	23	**56.7**	*14.7*	0	0
II-8	0.1	0.75	1.32	**1.66**	*1.00*	1.47	**28**	*2*	25	**56.2**	*8.5*	0	0
II-9	0.1	1.0	1.42	**1.48**	*0.88*	1.36	**31**	*2*	26	**54.8**	*6.4*	0	0

Numerals in bold indicate maximum values; numerals in italic indicate minimum values.

3.3.1. Variation of $\mu_{(P)}$ for 'silt' in experiment Ia

The highest shear stresses were always measured in the top layer, whilst the lowest values – with the exception of Ia-1 – were observed in the intermediate layer (Fig. 4a; Table 4). The increase of the strength ratios resulted in a decrease of the shear stress from 3.91 to 1.74 MPa and from 2.81 to 0.69 MPa for the top and bottom 'silt' layers, respectively. In addition, the increase of SR only caused a slight decrease of shear stress at the intermediate 'clay' from 1.5 to 0.92 MPa.

3.3.2. Variation of $\mu_{(P)}$ for 'clay' in experiment Ib

In this experiment, the measured shear stresses for the intermediate 'clay' ranged from 1.03 to 1.81 MPa (Fig. 4b; Table 4) and were always lower than the under and overlying 'silt' layers. The highest average shear stress was measured in the top 'silt' layer, except for experiments Ib-1,6,9 where it was observed in the bottom 'silt' layer. In these 'silt' layers the increase in the strength ratio SR also resulted in an overall increasing trend in the shear stress ranging from 1.81 to 3.34 MPa and 1.74 to 3.85 MPa for the bottom and top layers, respectively.

3.3.3. Variation of $\mu_{(P)}$ for 'clay' in experiment II

Compared to the 'silt'–'clay'–'silt' sequence, differences in the measured shear stress between the 'clay' layers were small (Fig. 4c; Table 4). For strength ratios <1.0 the shear stress at the intermediate layer ranged from 1.35 to 1.08 MPa and was higher in both the top and bottom layers. Low SR caused low shear stresses for the top and bottom layers ranging between 0.7 and 1.33 MPa. Then, for increasing SR >1.0, the shear stress values decreased at the intermediate layer, so that they were lower than the top and bottom layers. Hence, measured shear stress was always highest in those layers which were mechanically the weakest.

3.4. Sliding fraction, rolling and coordination number

3.4.1. Variation of $\mu_{(P)}$ of 'silt' in experiment Ia

3.4.1.1. Effects on the 'silt' layers. The gradual increase of the SR led to an increase in the sliding fraction of both 'silt' layers from ~2% to ~51% (Fig. 5a). The difference between the top and bottom 'silt' layers was negligible (~3%), except for experiments Ia-1 to Ia-3. In addition, increasing the SR also caused an increase in the extent of the rolling, so that more 'silt' particles rolled to higher degrees (Fig. 6a; Table 4).

3.4.1.2. Effects on the 'clay' layer. The variation of the SR had no significant effect on the sliding fraction of the intermediate 'clay' layer, where the sliding fraction varied around 26%.

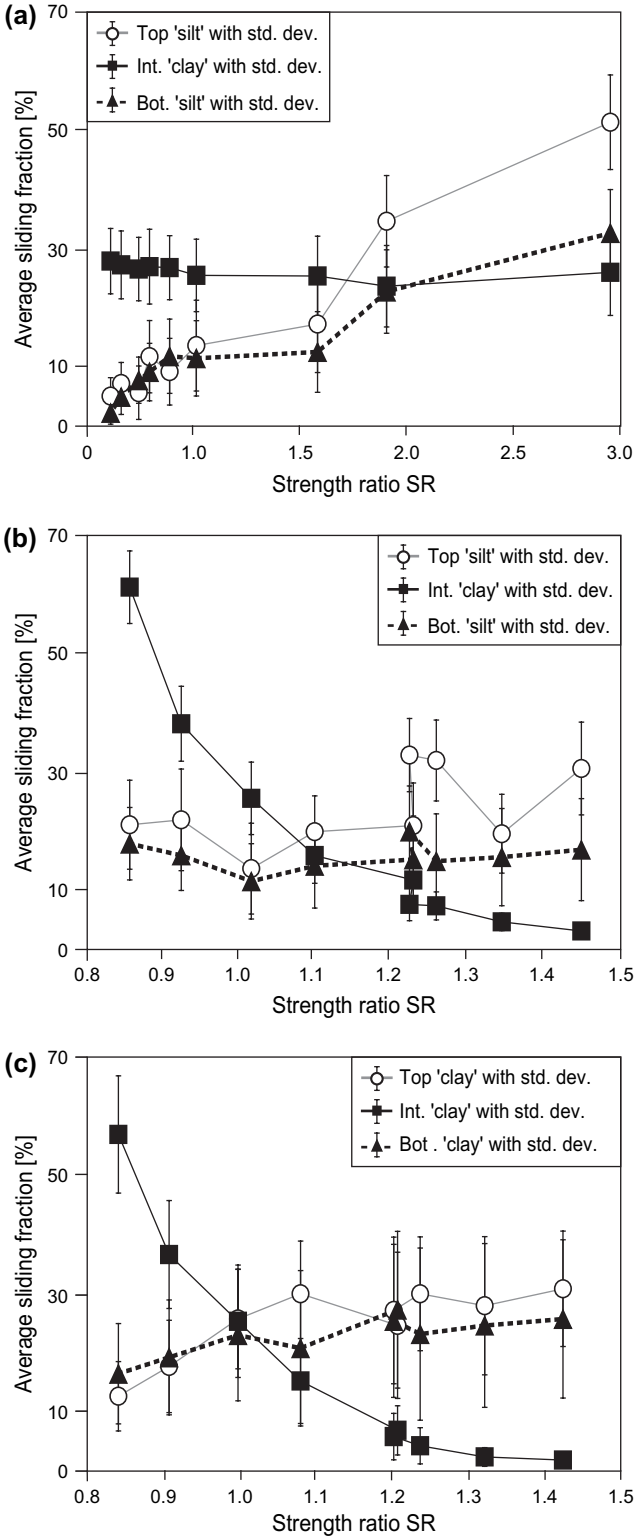

Fig. 5. Average sliding fraction vs. strength ratio SR. Average sliding fraction is the percentage of interparticle contacts which slide, calculated from 0% to 200 % strain. Circles denote sliding fraction for the top layer, squares for the intermediate layer, and triangles for the bottom layer. (a), (b), and (c) are same as Fig. 3.

Correspondingly, the magnitude of rotation of the 'clay' particles in the intermediate layer stayed almost constant (Fig. 6b; Table 4), except for when the SR was very low. If, however, the SR was very high (experiments Ia-1 and Ia-2) the number of contacts slipping in the intermediate 'clay' layer was lower than that in both the 'silt' layers.

3.4.2. Variation of $\mu_{(P)}$ for 'clay' in experiment Ib

3.4.2.1. Effects on the 'clay' layer. For very low strength ratios (SR < 1.0) the sliding fraction for the 'clay' was highest ranging from ~25% to ~61% (Fig. 5b; Table 4). When the SR increased to >1.1, the sliding fraction was lowest. Increase of the SR caused a general decrease in the rotation magnitude (Fig. 6d; Table 4), although values were almost constant over a wide range of SR.

3.4.2.2. Effects on the 'silt' layers. In contrast to experiment Ia, the influence of the SR (while changing the 'clay' properties) on the micromechanical properties of neighbouring layers increased (Fig. 5b; Table 4).

In contrast to previous experiments, the sliding fraction of the 'silt' showed no systematic trend in relation to the SR, instead it was highly variable. However, if the SR was >1.1, the sliding fraction of both the 'silt' layers was always higher than that of the intermediate layer. The magnitude of rolling for the 'silt' increased rapidly when the SR was increased, (Fig. 6c; Table 4). When the SR was at values >1.2, rolling showed a sharp drop, after which it varied around a mean percentage for each threshold angle.

3.4.3. Variation of $\mu_{(P)}$ of the intermediate 'clay' (experiment II)

3.4.3.1. Effects on the intermediate 'clay' layer. The sliding fraction decreased with increasing strength ratio from ~57% to ~2% (Fig. 5c; Table 4). When the top and bottom layers were mechanically weaker than the intermediate one (SR > 1), the sliding fraction of the intermediate layer immediately became smaller than the under and overlying layers and the rotation magnitude (Fig. 6f; Table 4) for the intermediate layer decreased.

3.4.3.2. Effects on the top and bottom 'clay' layers. An increase of the SR caused an increase in the sliding fraction to ~31%. For SR > 1, the sliding fraction of the top and bottom layers was highly variable, but always greater than that of the intermediate layer (Fig. 5c; Table 4). Correspondingly, the rotation magnitude increased for low to high strength ratios and remained almost constant for very high values of SR (Fig. 6e; Table 4).

4. Discussion

4.1. Localization patterns

Our results showed typical deformation structures that have also been observed in analogue tests (Maltman, 1994a; Marone, 1998; Scholz, 2002). Specifically, we interpret the observed slip planes (see Fig. 3, Section 3.2) as being similar to R_1, R_2, P, and Y fractures (e.g. Maltman, 1994b; Scholz, 2002; Fig. 3).

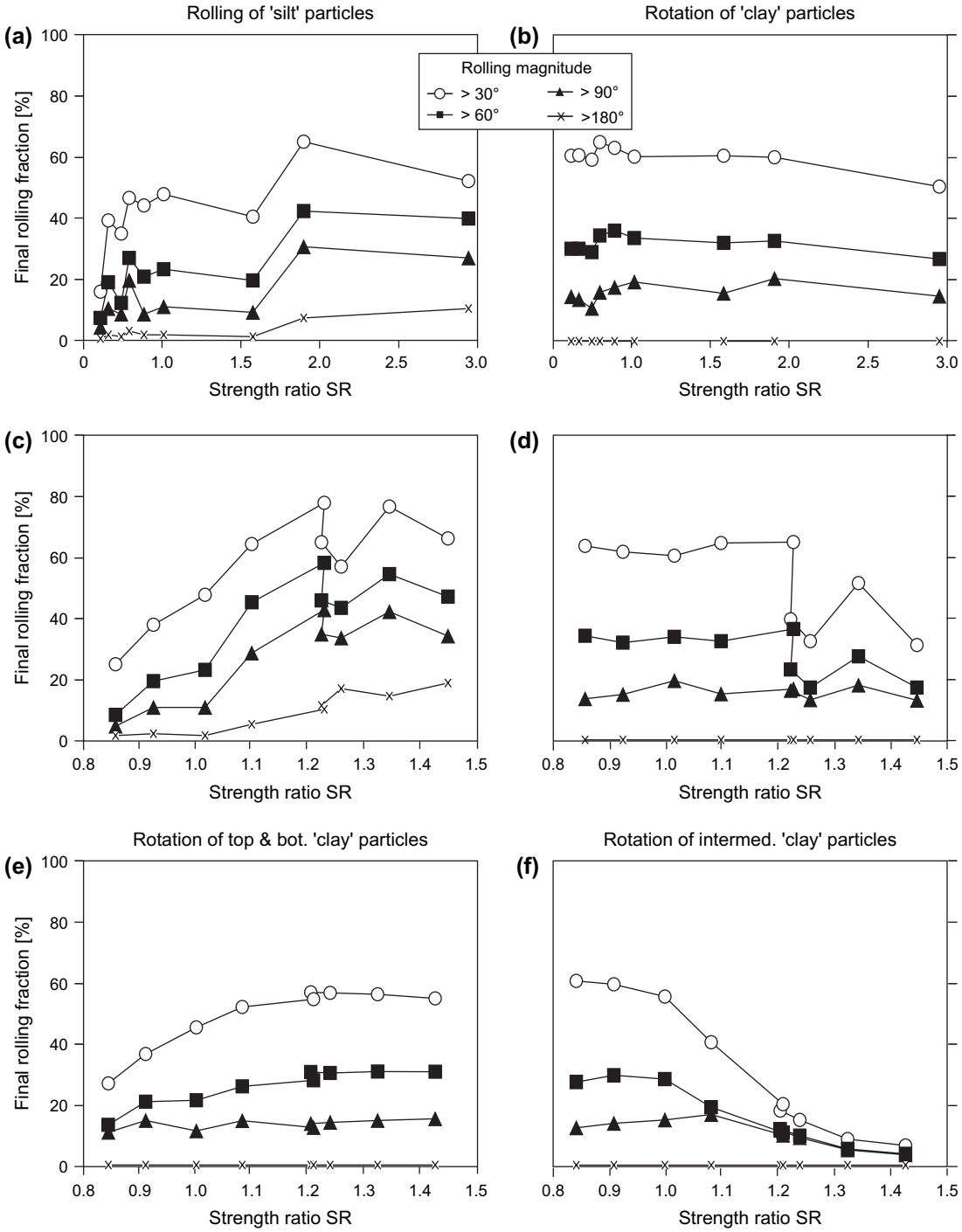

Fig. 6. Final (200% strain) rotation magnitude and fraction vs. strength ratio SR. At 0% strain, all particles had rotated 0°. At 200% strain: circles denote percentage of grains which rotated to angles >30°, squares denote percentage of grains which rotated to angles >60°, triangles denote percentage of grains which rotated to angles >90°, '*x*' denote percentage of grains which rotated to angles >180°. (a) and (b) are same as (a) in Fig. 3; (c) and (d) are same as (b) in Fig. 3; and (e) and (f) are same as (c) in Fig. 3.

Slip planes were not very well pronounced in the 'silts' in experiments Ia and Ib (Fig. 3a,i–ii, b,iv–v) which may be due to the low layer height and therefore the low particle number. Additionally, the slip plane length in the 'silt' is influenced more by particle diameter than in the 'clay'. It must also be kept in mind that the upper boundary wall induced shear stress on the specimen, so in the case of similar upper and lower layers, it is likely that localization will occur in the upper layer. Therefore, we only tentatively define slip planes corresponding to P and R_1 shears in the top 'silt' layers of these experiments (Fig. 3a,i–ii, b,iv–v). Similar structures have, however, been observed in other numerical studies (Morgan

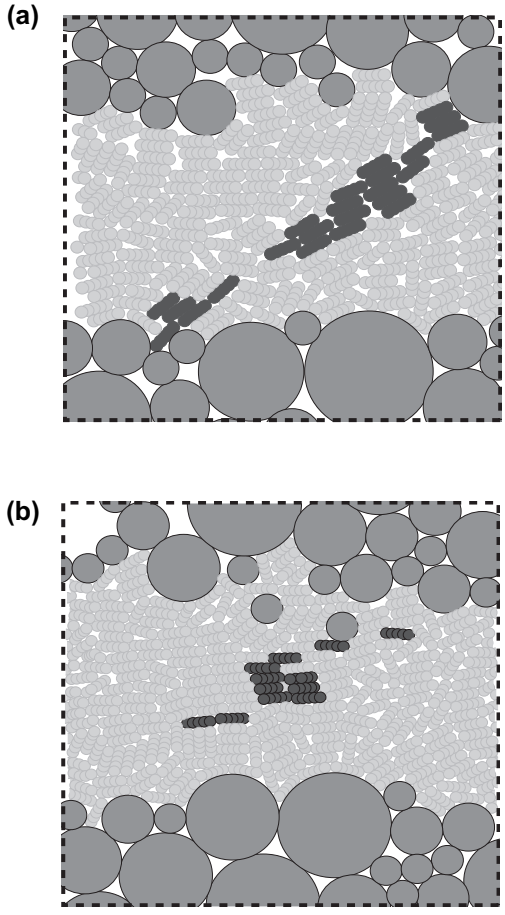

Fig. 7. Close-up particle configuration for selected models after 200% strain. Dark grey particles, 'silt'; medium grey particles, 'clay'. (a) Black particles show particle alignment corresponding to P-shears in Fig. 3a,v; experiment Ia-9. (b) Black particles show particle alignment corresponding to stair-step structure in Fig. 3b,i; experiment Ib-1.

and Boettcher, 1999; Kock and Huhn, 2007) as well as in natural specimens (Huhn et al., 2006) and are commonly defined as Riedel structures.

Localization features were generally more convincing in the 'clay' layers. P and R_1 fracture types were more pronounced in the 'clay' layers throughout all of the experiments. P-fractures extending over nearly the entire height of the 'clay' layer started to form with low strength ratios (Fig. 3a,iii–v, b,i–ii, c). As in nature (Rutter et al., 1986), this is an indication for particle alignment. An example of this is illustrated in Fig. 7a, where particle alignment and orientation enhanced slip and led to fractures along domains of oriented particles.

Usually, Y-shears are interpreted as accommodating large amounts of slip (Rutter et al., 1986; Scholz, 2002). Since our models achieved a strain of 200%, we would expect well-pronounced Y-shear planes in all of the experiments (Fig. 3) with the exception of experiment Ib (Fig. 3b,v), where this was not the case. We thus conclude that on a grain scale level, a single Y-plane may be exchanged for a collection of parallel oriented stair-step slip planes (e.g. Fig. 2c,i). Each step was oriented parallel to the shear box width, forming an assemblage of very small Y-shear planes. The complete step-like structure, however, seemed to be parallel to the P orientation (Fig. 2c,i; black ellipse) which is of interest because Y-planes are thought to deflect small scale (Rutter et al., 1986) and large scale (Maltman, 1994a) movement in the P-direction. On our microscopic scale, these stair-case structures indicate slip along or slip of a few 'clay' particles (Fig. 7b). This means that the mode of slip (Y or P) was controlled by only a few particles at the particle scale level whereas long Y-planes only developed if all the small scale Y-planes at each particle could connect together.

In a manner similar to natural materials (Rutter et al., 1986), R_2 slip planes occurred seldomly in our models. Examples of the R_2 orientation were observed in the stratified 'clay' experiment II (Fig. 3c,i). Morgan and Boettcher (1999) found R_2 structures in DEM models with circular particles, so the 'silt' layer height in our models may be too small to reproduce such features. However, in a similar experiment with a larger shear box we observed such features in the 'silts' (Kock and Huhn, 2007). In the 'clay' layer, the slip is clearly dominated by deformation structures above, so there seems to be no geometric requirement for R_2 fractures.

4.2. Micromechanics

Our results indicate that in stratified materials deformation modes of particles are influenced by differences in the mechanical strength of the neighbouring layers. Deformation at interparticle contacts occurs in two ways for circular particles: contact sliding or particle rotation. For a given shear force and angle acting at a contact, the extent of sliding depends on $\mu_{(P)}$ (Morgan, 1999). For circular particles, the sliding decreases with increasing $\mu_{(P)}$, whilst the particle rotation increases. These different mechanical strengths were achieved by varying the particle coefficient of friction. The resulting different amounts of sliding and rotation for the circular and elongated particles of each separate layer are therefore likely to control the observed localization features, i.e. localization in a layer or at layer boundaries.

Besides the influence of the $\mu_{(P)}$ on sliding and rotation, the shape of the particles in single layers also played a significant role in our models; circular particles may rotate whilst remaining at the same position during deformation (a process generally termed rolling). This is one reason that the presented shear stress results for the 'silt' (Table 2; Fig. 2) are low compared to natural systems and also to numerical models employing angular grains (Gao et al., 2004), for example, the rolling of platy 'clay' particles is restricted by their elongated shape. Instead the orientation of elongated particles only changes when there is enough space available for their long axis to rotate. This is mostly the case during the initial stage of deformation, when a complex microstructure is altered significantly due to particle reorientation. This process is associated with a decrease in the porosity and shear cell contraction (Kock and Huhn, 2007). In contrast, the deformation of circular particles

is usually associated with net dilation and it is apparent that this increases with particle friction (e.g. Morgan, 1999).

Between experiments Ia and Ib the same tendency to localize, even in mechanically stronger layers, could be observed (experiments Ia-1 to Ia-5 and Ib-3 to Ib-5), although the threshold levels of the strength ratio were different. In experiment Ia the threshold in order for deformation to localize extensively in the stronger 'clay' layer was SR = 1.58 compared to SR = 1.23 in experiment Ib. This indicates that in a layered material not only the mechanical strength governs the localization.

In experiment Ia, the 'silt' was the mechanically weak layer in several simulations (experiments Ia-1 to Ia-5). Nevertheless, the deformation was not always localized in this layer (experiments Ia-3 to Ia-5), instead shear deformation occurred by sliding and rolling of the 'silt' as indicated by the high sliding fraction and the high rolling percentage of experiments Ia-1 to Ia-2. The sudden decrease of the rolling and sliding of the 'silt' particles in experiment Ia-3 revealed that the sliding and rotation of the 'clay' was favoured, although the 'silt' was the weaker layer. The reason for this is that deformation of the 'silt' could not take place under a load of 5 MPa without increasing the layer dilation. This was shown by Morgan (1999), who argued that increasing the particle friction for circular particles leads to higher dilation. Accordingly, the progressive increase of the particle friction (i.e. lower strength ratios) would result in increasing dilation if only the 'silt' layer would solely deform. Deformation in the 'clay' was still possible via layer contraction, which is mainly due to particle rotation during the initial stages of deformation (Kock and Huhn, 2007). Because the contraction is mechanically simpler to achieve and thereby more favourable than dilation, deformation was localized in the mechanically stronger layer.

In the case of the low SR (<1.0) experiments Ia-6 to Ia-9, the intermediate layer always acted as a decoupling layer and the deformation did not extend as far as the lower 'silt' layer. Consequently, shear stress acting at the particles in the lower layer could not be as high as in the upper layer. Both of the 'silt' layers in these cases were non-failing during simulation, although some residual sliding at particle contacts always occurred as the non-zero values of the sliding fraction indicate. With increasing $\mu_{(P)}$, the 'silt' particle assemblage achieved enhanced stability, which reduced the slip greatly and had only a slight effect on the rolling. Thus, the upper layer essentially moved as block in the positive x-direction whilst single particles could bear high shear stress values.

In experiment Ib the connection between the strength ratio and localization was straightforward for the end-members in the model suite. Deformation occurred in the layer that was weakest mechanically. For very low SR, deformation was localized in the intermediate 'clay' and for very high SR deformation occurred in the upper 'silt' as displacement plots in Fig. 3 and the sliding fraction indicate.

Experiments Ib-4 to Ib-5 are more interesting, since deformation was not localized strictly in the weakest layer, but distributed along the boundary in both layers and did not form a sharp discontinuity. This also coincided with a slight increase of the rotation for the 'clay' (albeit only for relatively low angles) and of rolling for the 'silt'. It is questionable which one of these layers failed initially, since deformation was localized in both, but most probably it was the mechanically weak 'silt' layer.

When both of the particle types moved extensively, layers started to mix (Fig. 8a). This mixing of the layers also occurred for experiment Ia-1,2 (Fig. 8b). The common characteristics of experiments Ia-1,2 and Ib-4,5 (despite the 'silt' being mechanically weak) are high rolling and rotation magnitudes (e.g. >50% for 30°) both in the top 'silt' and in the 'clay'. Rotation of the 'clay' particles is especially active in the initial stages of the experiment (Kock and Huhn, 2007) and the particle friction of the 'clay' was still relatively low, so the stability of this layer was not extremely high (Thornton, 2000). Particle rotation of the 'clay' then led to contraction during deformation, in a similar manner to the homogenous assemblages reported in Kock and Huhn (2007). In contrast to the above, and in a similar manner to experiment Ia-1,2, a 'silt' layer is likely to dilate during deformation. Since the 'silt' was the mechanically weak layer it is probable that deformation started in that layer, but both of the particle types could easily roll and rotate. Thus, layer mixing and distributed deformation developed along the layer boundary.

For the subsequent experiments Ib-6 to Ib-9, the enhanced stability of the platy 'clay' particles with increasing particle friction (Thornton, 2000) and the resulting sudden decrease of 'clay' particle rotation (Fig. 6d) prohibited layer mixing. Hence, the deformation was not distributed along the boundary, but localized directly at the boundary so that a long distinct shear plane evolved (Fig. 3b,v). Similar to experiment Ia, localization of the deformation never reached the bottom layer, since decoupling occurred well above it.

Because the particle shape was identical for all layers in the pure 'clay' experiment, only 'clay' sliding and rotation played a role during shear. The localization consequently occurred in the layers where the strength and $\mu_{(P)}$ were the lowest, and where the sliding fraction and the rotation magnitude were the highest. In the pure clay experiment decoupling occurred in the intermediate layer for SR < 1.0, in the top and intermediate layer for SR = 1.0 and in the top layer only when the SR was highest. Accordingly, the shear stresses were low in the bottom layer and also in the intermediate layer when SR > 1.0.

There existed one case where the localization was not only observed in the top 'clay', but also in the bottom 'clay'. Accordingly, decoupling did not occur in the top or intermediate layer during this simulation.

A sliding fraction $>\sim$30% for a layer indicated localization along the shear planes (Fig. 5c). Furthermore, when more than 40% of particles rotated more than 30°, localization occurred via particle reorientation (Fig. 6e–f). Sliding and rotation are dominant during the different stages of deformation. Rotation is initially important, when the 'clay' microstructure disaggregates, later, particle alignment has progressed to such an extent that the particle sliding is enhanced and becomes the dominant process. Therefore, the alignment of particles produced structures which are also observed in nature, such as

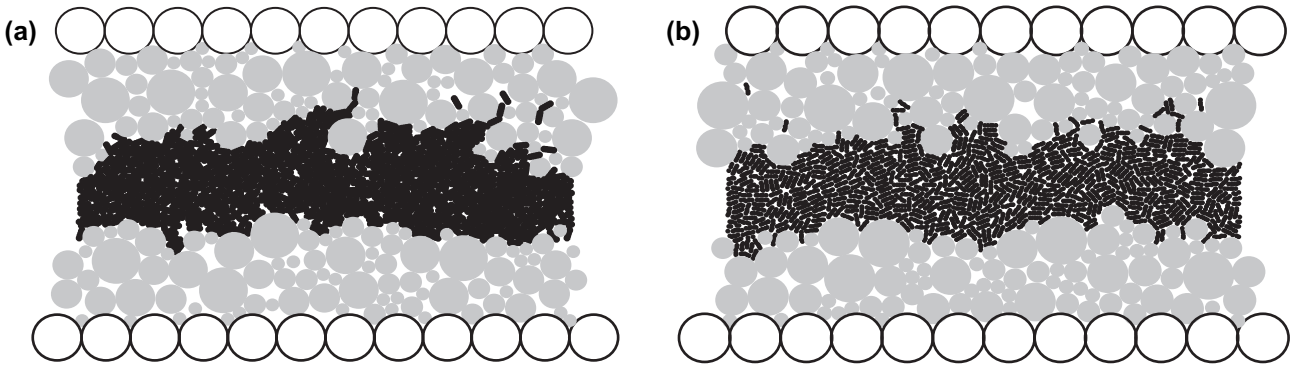

Fig. 8. Particle configuration after 200% strain for selected model runs. Black line indicates top layer boundary. Black particles, 'clay'; grey particles, 'silt'; white particles, 'walls'. After 200% strain, layer boundaries are blurred. 'Clay' particles have slid into gaps between 'silt' particles. (a) SR = 1.10; experiment Ib-4. (b) SR = 1.91; experiment Ia-2.

the clay mineral domains defined by preferred orientations (Bennett et al., 1991; Mitchell and Soga, 2005).

4.3. Implications for natural materials

In the cases of experiment I, where deformation took place primarily in the 'clay' layers, displacement was distributed throughout the layer. On the grain scale level in natural sheared clays, we would thus expect a multitude of possible slip planes with minimal displacement rather than a narrow slip plane where a large part of the displacement accumulated. This network of slip planes is similar to the microscopic appearance in scaly clays (e.g. Vanucchi et al., 2003).

There are several experiments where the shear was located not exclusively in the 'clay' layer, but where the displacement was localized at least partially or almost exclusively in the top 'silt' layer (Fig. 3a,i–ii, b,iii–v). In the former case, the displacement and shear were distributed across the layer boundary and within the layers. In general, natural situations where SR > 1.0 so that $\mu_{(P),\text{'silt'}} < \mu_{(P),\text{'clay'}}$ may be rare, but scenarios

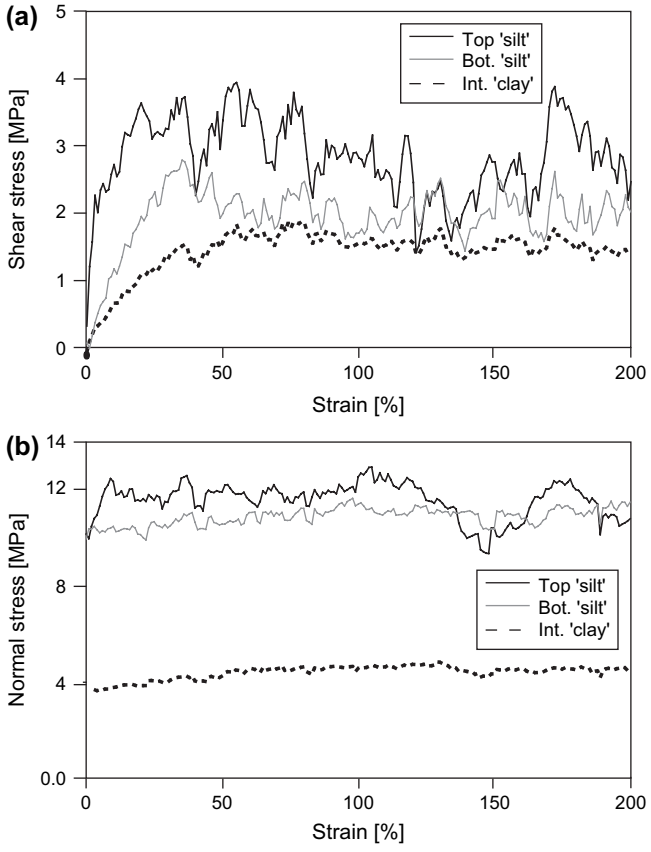

Fig. 9. Magnitudes and variations of shear and normal stresses in stratified assemblage (experiment Ia-3, $\mu_{(P)}$ 0.1 for 'silt' and 'clay'). Black solid line indicates top 'silt', grey solid line indicates bottom 'silt', black dashed line indicates intermediate 'clay'. (a) Shear stress. (b) Normal stress.

where loose soil overlies cemented clay or welded volcanic ash may be conceivable. To this regard, Sperrevik et al. (2000) showed that the development of clay smears depends on the competence contrast between sands and clays. This may be applicable to our results although their testing setup is different from ours in the respect that they use a vertical slab of clay in loose sand as their soil specimen. The latter case represents an end-member of our experiments and its occurrence in natural systems is rare. However, cases where the contact between layers acts as the weak part during shear have been described in the literature (Hatzor and Levin, 1997).

One of the most interesting features of experiment II is its sensitivity to small changes in the particle properties. The shift from SR < 1.0 to SR > 1.0 led to a complete change in the localization features (Fig. 2c,i–iii), although the absolute change in the strength and in the particle friction was small. For natural clay such a result indicates that even small changes in, for example, mineral composition or cementation could result in highly different displacement and localization patterns. Such a process could explain deformation processes where the shear localization occurred only in defined areas of a complex clayey lithology, such as the Barbados prism decollement (Labaume et al., 1997; Maltman et al., 1997) or for microscopic scale S–C band formation in clays (Labaume et al., 1997; Takizawa and Ogawa, 1999).

5. Conclusions

We conducted numerical DEM simulations on two types of layered specimen: (1) a 'silt'–'clay'–'silt' assemblage and (2) a 'clay'–'clay'–'clay' package. Mechanical strength of each layer was varied by systematically changing the coefficient of particle friction. The differences in strength between the layers led to distinctly different localization and micromechanical deformation characteristics:

- It is known that localization is a complicated mechanism on the grain scale level. Our stratified models confirm this and reveal that localization of the deformation mostly occurs inside a weak layer, but that there are also several cases where localization emerges at layer boundaries and even extends into adjacent layers. The modes of deformation are particle sliding and rotation and the amount to which each of these deformation modes occurs is governed by contrasting particle friction and by the differences in strength of the layers.

Therefore, the capacity of different layers to dilate or contract during deformation may take precedence over the pure mechanical strength. Thus, localization is in some cases observed in a mechanically strong layer with the opportunity to contract rather than in a weak layer which has to dilate during deformation.

- For an intermediate, mechanically weak 'clay', the deformation was strictly localized inside the clay when the sliding and rotation of the elongated 'clay' particles could be high, which is the case for low coefficients of particle friction for the 'clay'. The level of the coefficient of particle friction for the 'silt' did not play a role in these cases.
- For an intermediate, mechanically weak 'clay', deformation was distributed around the 'clay'/'silt' boundary when rotation of both particle types could be high and when the 'silt' had to dilate strongly to deform. This is the case for intermediate coefficients of particle friction for the 'clay' and 'silt'.
- For an intermediate, mechanically weak 'clay', deformation concentrated directly at the 'clay'/'silt' boundary when the rotation of the 'clay' was low, which was the case when the coefficients of particle friction for the 'clay' were high.
- Decoupling was observed in most of the simulations, so that deformation did not extend down into the bottom layer.
- The observed localization structures showed a remarkable similarity to natural sediments. Classical Riedel structures on the grain scale level allow microscopic deformation to be observed. In some cases features that might develop into Y-shears were observed, while P and R1 type shear planes were abundant in all models. Additionally, the 'clay' type material shows a distinct connection between the slip planes and the particle alignment.
- Comparing the model with natural systems showed in general some interesting correlations to features observed in scaly clays and similarities to S–C band formation. This implies that the micromechanical behaviour we observed is applicable. Nevertheless, there is a wide range of features during sediment deformation which could not be captured by our models. Grain breakage, fluid involvement and three-dimensionality certainly influence deformational behaviour of rocks and need further analysis.

Acknowledgements

Funding for this research has been received through the Deutsche Forschungsgemeinschaft via the Research Center Ocean Margins (RCOM). This is RCOM publication #0520.

We thank two anonymous reviewers who greatly helped to improve the manuscript. We owe many thanks to our colleagues Achim Kopf and Dave Heslop from the Research Center Ocean Margins for advice and discussions on an earlier version of the manuscript.

Appendix.

To judge variation of shear and normal stress during deformation results of stress calculation are shown in Fig. 9a,b. Note that shear and normal were calculated as the average shear and normal stress acting on all particles in a respective layer. Therefore, the calculated normal stress presented here does not equal to the applied normal stress. There are two main factors which are responsible for the difference.

First, in a granular particle assembly, the total stress tensor in a defined volume V can be calculated with

$$\overline{\sigma}_{ij}^{(M)} = \frac{1}{V}\sum_{n} \sigma_{(P),ij} \times V_{(P)}, \quad i = 1,2;\ j = 1,2 \tag{1}$$

or, alternatively

$$\overline{\sigma}_{ij}^{(M)} = \left(\frac{1-\nu}{\sum_{n} V_{(P)}}\right) \sum_{n} \sigma_{(P),ij} \times V_{(P)}, \quad i = 1,2;\ j = 1,2 \tag{2}$$

where $\sigma_{(P),ij}$ is the stress tensor for a single particle, $V_{(P)}$ the particle volume and n the particle number and ν the porosity within the defined volume (Itasca, 2004).

Results presented here depend only on particle stress, i.e. are calculated by averaging $\sigma_{(P),ij}$ and do not consider void space or layer volume. Reason for this is the difficulty to accurately compute layer volume V and/or layer porosity ν at each step during simulation.

Secondly, contact force distribution in granular assemblies is a much debated topic (e.g. Radjai et al., 1998). Thus, taking the average may not accurately represent the stress state in a granular assemblage.

The consequences of this approach can be seen in Fig. 9b. Average normal stress for the 'silt' layers was much higher than for the 'clay'. One component for high stress certainly was the visibly higher porosity of the 'silt' layer (e.g. Fig. 8a,b). The other reason for these high values was the heterogenous distribution of contact forces. In a granular assembly, forces are transmitted via strong and weak networks, where the strong network consists of few contacts with high force magnitudes. In the 'silt' layer the low number of particles resulted in few contacts with extremely high forces. Hence, high normal stress magnitude displayed in Fig. 9b developed. Another consequence of low particle number for the 'silt' is the relatively high variation of shear and normal stress curve when compared to 'clay'. The formation and destruction of single contacts with associated forces have more impact on average particle stress for low than for high particle numbers.

References

Antonellini, M.A., Pollard, D.D., 1995. Distinct element modelling of deformation bands in sandstone. Journal of Structural Geology 17 (8), 1165–1182.

Ask, M.V.S., Kopf, A., 2004. Constraints on the state of in situ effective stress and the mechanical behaviour of ODP Leg 186 claystones in the Japan Trench forearc. The Island Arc 13 (1), 242–257.

Bennett, R.H., Bryant, W.R., Hulbert, M.H., 1991. Microstructure of Fine-grained Sediments. In: Bouma, A.H. (Ed.), Frontiers in Sedimentology. Springer-Verlag, New York, p. 582.

Canals, M., Lastras, G., Urgeles, R., Casamor, J.L., Mienert, J., Cattaneo, A., De Batist, M., Haflidason, H., Imbo, Y., Laberg, J.S., Locat, J., Long, D., Longva, O., Masson, D.G., Sultan, N., Trincardi, F., Bryn, P., 2004. Slope failure dynamics and impacts from seafloor and shallow sub-seafloor geophysical data: case studies from the COSTA project. Marine Geology 213, 9–72.

Cundall, P.A., 1989. Numerical experiments on localization in frictional materials. Ingenieur-Archiv 59, 148–159.

Cundall, P.A., Strack, O.D.L., 1978. BALL – a program to model granular media using the distinct element method. Technical Note. Advanced Technology Group, Dames and Moore, London.

Cundall, P.A., Strack, O.D.L., 1979. A discrete numerical model for granular assemblies. Géotechnique 29 (1), 47–65.

Cundall, P.A., Strack, O.D.L., 1983. Modeling of microscopic mechanisms in granular material. In: Jenkins, J.T., Satake, M. (Eds.), Mechanics of Granular Materials: New Models and Constitutive Relations. Elsevier Science Publishers B.V, Amsterdam.

Dahlen, F.A., 1984. Noncohesive critical Coulomb wedges: an exact solution. Journal of Geophysical Research 89 (B12), 10125–10133.

Füchtbauer, H., 1988. Sedimente- und Sedimentgesteine. E.Schweizbart'sche Verlagsbuchhandlung, Stuttgart. 1141.

Gao, J., Luedtke, D., Gourdon, D., Ruths, M., Israelachvilli, J., Landman, U., 2004. Frictional forces and Amontons' law: from the molecular to the macroscopic scale. Journal of Physical Chemistry B 108, 3410–3425.

Guo, Y., Morgan, J.K., 2004. Influence of normal stress and grain shape on granular friction: results of discrete element simulations. Journal of Geophysical Research 109, B12305, doi:10.1029/2004JB003044.

Hampton, M.A., Lee, H.J., Locat, J., 1996. Submarine landslides. Reviews of Geophysics 34 (1), 33–59.

Hatzor, Y.H., Levin, M., 1997. The shear strength of clay-filled bedding planes in limestones – back-analysis of a slope failure in a phosphate mine, Israel. Geotechnical and Geological Engineering 15, 263–282.

Hazzard, J.F., Mair, K., 2003. The importance of the third dimension in granular shear. Geophysical Research Letters 30 (13), 1708, doi:10.1029/2003GL017534.

Huhn, K., Kock, I., Kopf, A., 2006. Comparative numerical and analogue shear box experiments and their implications for the mechanics along the failure plane of landslides. Norwegian Journal of Geology 86 (3), 209–220.

Itasca, 2004. PFC 2D 3.1 Manual. Itasca Consulting Group, Inc, Minneapolis.

Jaeger, H.M., Nagel, S.R., Behringer, R.P., 1996. Granular solids, liquids and gases. Reviews of Modern Physics 68 (4), 1259–1273.

Kock, I., Huhn, K., 2007. Influence of particle shape on the frictional strength of sediments – a numerical case study. Sedimentary Geology 196 (1–4), 217–233, doi:10.1016/j.sedgeo.2006.07.011.

Kopf, A., Brown, K.M., 2003. Friction experiments on saturated sediments and their implications for the stress state of the Nankai and Barbados subduction thrusts. Marine Geology 202 (3–4), 193–210.

Labaume, P., Maltman, A.J., Bolton, A., Tessier, D., Ogawa, Y., Takizawa, S., 1997. Scaly fabrics in sheared clays from the décollement zone of the Barbados accretionary prism. In: Shipley, T.H., Ogawa, Y., Blum, P., Bahr, J.M. (Eds.), Proceedings of ODP, Scientific Results, 156. Ocean Drilling Program, College Station, TX, pp. 59–78.

Lupini, J.F., Skinner, A.E., Vaughan, P.R., 1981. The drained residual strength of cohesive soils. Geotechnique 31 (2), 181–213.

Mair, K., Frye, K.M., Marone, C., 2002. Influence of grain characteristics on the friction of granular shear zones. Journal of Geophysical Research 107 (B10), 2219, doi:10.1029/2001JB000516.

Maltman, A., 1994a. Deformation structures preserved in rocks. In: Maltman, A. (Ed.), The Geological Deformation of Sediments. Chapman & Hall, London, p. 392.

Maltman, A., 1994b. The Geological Deformation of Sediments. Chapman & Hall, London. 362.

Maltman, A., Labaume, P., Housen, B., 1997. Structural geology of the décollement at the toe of the Barbados accretionary prism. In: Shipley, T.H., Ogawa, Y., Blum, P., Bahr, J.M. (Eds.), Proceedings of ODP, Scientific Results, 156. Ocean Drilling Program, College Station, TX, pp. 279–292.

Marone, C., 1998. Laboratory-derived friction laws and their application to seismic faulting. Annual Review of Earth and Planetary Sciences 26, 643–696.

Mitchell, J.K., Soga, K., 2005. Fundamentals of Soil Behaviour. John Willey & Sons, Hoboken, New Jersey.

Morgan, J.K., 1999. Numerical simulations of granular shear zones using the distinct element method 2. Effects of particle size distribution and interparticle friction on mechanical behaviour. Journal of Geophysical Research 104 (B2), 2721–2732.

Morgan, J.K., Boettcher, M.S., 1999. Numerical simulations of granular shear zones using the distinct element method 1. Shear zone kinematics and the

micromechanics of localization. Journal of Geophysical Research 104 (B2), 2703–2719.

Oda, M., Iwashita, K., 1999. Mechanics of Granular Materials. A.A. Balkema, Rotterdam/Brookfield.

Radjai, F., Wolf, D.E., Jean, M., Moreau, J.-J., 1998. Bimodal character of stress transmission in granular packings. Physical Review Letters 80 (1), 61–64.

Rutter, E.H., Maddock, R.H., Hall, S.H., White, S.H., 1986. Comparative microstructures of natural and experimentally produced clay-bearing fault gouges. Pure and Applied Geophysics 124, 3–30.

Saffer, D.M., Frye, K.M., Marone, C., Mair, K., 2001. Laboratory results indicating complex and potentially unstable frictional behaviour of smectite clay. Geophysical Research Letters 28 (12), 2297–2300.

Saffer, D.M., Marone, C., 2003. Comparison of smectite- and illite-rich gouge frictional properties: application to the updip limit of the seismogenic zone along subduction megathrusts. Earth and Planetary Science Letters 25 (1–2), 219–235.

Scholz, C.H., 2002. The Mechanics of Earthquakes and Faulting. Cambridge University Press, Cambridge.

Schöpfer, M.P.J., Childs, C., Walsh, J.J., 2006. Localization of normal faults in multilayer sequences. Journal of Structural Geology 28 (5), 816–833.

Sperrevik, S., Faerseth, R.B., Gabrielsen, R.H., 2000. Experiments on clay smear along faults. Petroleum Geoscience 6 (2), 113–123.

Takizawa, S., Ogawa, Y., 1999. Dilatant clayey microstructure in the Barbados décollment zone. Journal of Structural Geology 21, 117–122.

Thornton, C., 2000. Numerical simulation of deviatoric shear deformation of granular media. Geotechnique 50 (1), 43–53.

Tucker, M.E., 1981. Sedimentary Petrology. Blackwell Scientific Publications, Oxford.

Vanucchi, P., Maltman, A., Bettelli, G., Clennell, B., 2003. On the nature of scaly fabric and scaly clay. Journal of Structural Geology 25, 673–688.

Wessel, P., Smith, W.H.F., 1991. Free software helps map and display data. EOS Transactions, American Geophysical Union 72, 441.